ADVANCES IN ATMOSPHERIC SCIENCES, VOL. 41, JANUARY 2024, 155–172

• **Original Paper** •

Mechanism of Diabatic Heating on Precipitation and the Track of a Tibetan Plateau Vortex over the Eastern Slope of the Tibetan Plateau

Yuanchang DONG[1], Guoping LI[*2], Xiaolin XIE[3], Long YANG[4], Peiwen ZHANG[1], and Bo ZENG[1]

[1]*Institute of Plateau Meteorology, China Meteorological Administration (CMA) / Heavy Rain and Drought-Flood Disaster in Plateau and Basin Key Laboratory of Sichuan Province, Chengdu* 610072, *China*

[2]*School of Atmospheric Sciences, Chengdu University of Information Technology, Chengdu* 610225, *China*

[3]*Meteorological Observation Data Center of Sichuan Province, Chengdu* 610072, *China*

[4]*Sichuan Branch of Meteorologist Training Institute, CMA, Chengdu* 610072, *China*

(Received 25 September 2022; revised 7 April 2023; accepted 10 April 2023)

ABSTRACT

Existing studies contend that latent heating (LH) will replace sensible heating (SH) to become the dominant factor affecting the development of the Tibetan Plateau vortex (TPV) after it moves off the Tibetan Plateau (TP). However, in the process of the TPV moving off the TP requires that the airmass traverse the eastern slope of the Tibetan Plateau (ESTP) where the topography and diabatic heating (DH) conditions rapidly change. How LH gradually replaces SH to become the dominant factor in the development of the TPV over the ESTP is still not very clear. In this paper, an analysis of a typical case of a TPV with a long life history over the ESTP is performed by using multi-sourced meteorological data and model simulations. The results show that SH from the TP surface can change the TPV-associated precipitation distribution by temperature advection after the TPV moves off the TP. The LH can then directly promote the development of the TPV and has a certain guiding effect on the track of the TPV. The SH can control the active area of LH by changing the falling area of the TPV-associated precipitation, so it still plays a key role in the development and tracking of the TPV even though it has moved out of the main body of the TP.

Key words: eastern slope of the Tibetan Plateau, diabatic heating, Tibetan Plateau vortex, precipitation distribution, track

Citation: Dong, Y. C., G. P. Li, X. L. Xie, L. Yang, P. W. Zhang, and B. Zeng, 2024: Mechanism of diabatic heating on precipitation and the track of a Tibetan Plateau vortex over the eastern slope of the Tibetan Plateau. *Adv. Atmos. Sci.*, **41**(1), 155−172, https://doi.org/10.1007/s00376-023-2275-7.

Article Highlights:

- Few studies have focused on how latent heating (LH) gradually replaced sensible heating (SH) as the dominant factor in the development of the Tibetan Plateau vortex (TPV) over the eastern slope of the Tibetan Plateau. The research results of this paper answered this question.
- The SH from the Tibetan Plateau (TP) surface has a significant effect on the track of the TPV even though it has moved off the TP.
- This study reveals the synergistic effect of SH and LH on the development and tracking of the TPV and points out that SH from the TP surface can affect the TPVs direction of movement by altering the distribution of the TPV-associated precipitation.

1. Introduction

Tibetan Plateau vortices (TPVs) are mesoscale shallow weather systems that generate over the Tibetan Plateau (TP) at the 500-hPa level. Its occurrence and development are closely related to the unique dynamic and thermal environment of the TP. Statistical results showed that TPVs occur and develop throughout the year, especially from June to September (Liu and Fu, 1986). TPVs are the main precipitation systems that originate from the TP in summer. Although the vast majority of TPVs cannot move off the TP, a few of them can move off the TP into the downstream areas (especially over the Sichuan Basin) under favorable cir-

* Corresponding author: Guoping LI
Email: liguoping@cuit.edu.cn

culation conditions, causing large-scale heavy rain, thunderstorms, and other disastrous weather processes (Ye, 1979; Luo, 1989; Chen et al., 2012; Zhang et al., 2014; Lin et al., 2021, 2022). Due to the significant and extensive weather impacts related to the TPVs, relevant research endeavors have been gradually enriched since the first Qinghai-Xizang Plateau Meteorological Experiment.

Heavy precipitation associated with a TPV is the main cause of disastrous weather, so the distribution characteristics and development mechanism of TPV-associated precipitation have been widely studied in research and weather forecasting. The intensity and distribution characteristics of TPV-associated precipitation are closely related to the occurrence and development characteristics of the TPVs themselves. Therefore, it is very important to understand the main factors affecting the occurrence and development of TPVs to accurately predict TPV-associated precipitation. Existing research results showed that the large-scale topography, surface heat flux, and latent heating (LH) related to condensation are important factors affecting the occurrence and development of TPVs (Chen et al., 1996a; Wu et al., 2018). The TP is a powerful heating source for the atmosphere of the northern hemisphere during the summer half of the year. Due to the high altitude of the TP, the ground sensible heating (SH) and LH over TP can directly heat the mid-troposphere and subsequently affect the weather and climate of China (Li et al., 2008). The surface SH of the TP plays a key role in the occurrence and development of TPVs (Tian et al., 2015). Dong and Li (2015) pointed out that the development of a TPV before moving off the TP is mainly affected by SH from the TP, while after moving off the TP, its development is mainly affected by LH. The main reason for this transformation is that the precipitation intensity often increases significantly once TPVs move off the TP, and the LH generated by a large amount of water vapor condensation becomes an important factor for the maintenance and structural evolution of TPVs (Song and Li, 2011). At the same time, after TPVs move off the TP, the distance between their height and the underlying surface increases sharply, and SH from the ground is greatly weakened. Therefore, the change in LH dominates the development of TPVs after they move off the TP.

After many years of research, we have reached more consensus on the different roles of SH and LH in different development stages of TPVs. The studies of Chen et al. (1996a) and Song et al. (2012) showed that SH (LH) mainly plays a role in the initial (development) stage of TPVs. Luo and Yang (1992) pointed out that the influence of diabatic heating (DH) can surpass that of dynamic processes and become the primary factor for the occurrence of TPVs, and further believed that the surface SH contributes the most to the DH. The research results of Dell'Osso and Chen (1986) and Shen et al. (1986) all demonstrated the importance of LH in the development of a TPV.

The summary of existing research results reveals that the importance of different DH forms in different stages of TPVs is fully understood, yet, despite such comprehension, the relationship between SH and LH in the development of TPVs has rarely been studied. The importance of SH and LH to the development of TPVs is mainly based on whether a TPV moves off the TP, noting that a TPV needs to pass over the eastern slopes of the TP (ESTP) when it moves eastward off the TP. There is a 3500-m elevation difference from the main body of the TP to the Sichuan Basin. The abrupt elevation change combined with the abrupt change of the surface SH, makes this region the most critical area for the development of the TPVs. Nearly 80% of the TPVs will die out near or to the west of this region (Yu and Gao, 2019). So how does DH affect the TPVs over this region, and what is the nature of the relationship between different forms of DH in the TPV developmental process become urgent questions to be answered.

In this paper, a typical case of a TPV that developed over the ESTP for 156 hours is used to reveal the DH mechanisms on the precipitation and track of the TPV after it moved off the TP, which provides a reference for scientific cognition and accurate prediction of the intensity and distribution of the TPVs-associated precipitation over the ESTP. The data and methods utilized in this work are introduced in section 2. In section 3, the climatic distribution characteristics of the 500-hPa temperature over the ESTP and the influence of the TPV on the temperature distribution over this region are discussed. The mechanisms of different forms of DH on the precipitation distribution and the track of the TPV are analyzed in section 4. Section 5 provides a conclusion and discussion.

2. Data and methods

2.1. *Datasets*

The data used and their functions mainly include the following.

(1) The geographical location, the track of the TPV, and the characteristic of wind, temperature, humidity, and potential vorticity are analyzed by using the ERA5 reanalysis hourly data (Hersbach et al., 2020) with a horizontal resolution of 0.5° × 0.5° during 1–31 July 2010.

(2) Radar echo characteristics of precipitation are analyzed by using the radar mosaic combination reflectivity (RMCR) data with a horizontal resolution of 1 km × 1 km and a six-minute temporal interval. The RMCR data were derived from raw data observed by fourteen CMA operational Doppler radars located at Mianyang (MY), Chengdu (CD), Nanchong (NC), Guangyuan (GY), Hanzhong (HZ), Yibin (YB), Wanxian (WX), Longnan (LN), Baoji (BJ), Xian (XA), Shiyan (SY), Yichang (YC), Jinzhou (JZ), and Xiangyang (XY) (Fig. 1) during 23–24 July 2010. The RMCR data can make up for the limitation of a single radar detection range (Xiao and Liu, 2006) and improve the data quality in the complex terrain area.

(3) The intensity and distribution of precipitation are studied by using the data observed by automatic weather system (AWS) with more than 2500 stations on the ESTP and its

vicinity during 21–26 July 2010.

(4) The Black Body Temperature (TBB) data (http://data.nsmc.org.cn) are obtained from the FengYun-2E (FY-2E) meteorological satellite with a spatial (temporal) resolution of 0.1° × 0.1° (1 h). TBB is used to characterize the temperature of the cloud top and measured the exuberance of convective development.

(5) The track of the TPV is obtained from the TPV yearbook for the year 2010 (IPM and CMA, 2010) and the objective database of TPVs derived from multiple reanalysis datasets (MRD) provided by Lin et al. (2020, http://data.tpdc.ac.cn/).

2.2. *Methodology*

Yanai et al. (1992) first proposed the inverse algorithm of DH rate (Eq. 1), which has been widely used because of the convenience of calculation and the parameters of calculation satisfied the balance of atmospheric energy and matter (Yao and Sun, 2013, 2016; Xu et al., 2014).

$$Q = \frac{\partial T}{\partial t} + \mathbf{V}\cdot\nabla T + \omega\left(\frac{p}{p_0}\right)^{\kappa}\frac{\partial\theta}{\partial p} = Q_t + Q_h + Q_v\,, \quad (1)$$

where Q is the DH rate [DH (diabatic cooling) when $Q >$ 0(<0)], θ is the potential temperature, T is the air temperature (units: K), p is the air pressure, p_0 = 1000 hPa,$\mathbf{V}$ is the horizontal wind vector, ω is the vertical velocity (units: Pa s^{-1}). Q_t, Q_h, and Q_v are the local variation, advection, and vertical transport terms of DH, respectively.

The DH can be further subdivided into its dry and moist counterparts:

$$Q_1 = Q\times C_p\,, \quad (2)$$

$$Q_2 = -L\left(\frac{\partial q}{\partial t} + \mathbf{V}\cdot\nabla q + \omega\cdot\frac{\partial q}{\partial p}\right), \quad (3)$$

where Q_1 is the apparent heat source and Q_2 is the apparent moisture sink, C_p is the specific heat capacity of dry air at constant pressure (1004.8 J kg^{-1} K^{-1}), L is the coefficient of latent heat of condensation (L= 2.5 × 10^6 J kg^{-1} when the temperature = 0°C).

2.3. *Model description and experimental design*

In this paper, the Weather Research and Forecasting Model (WRF) is used to simulate the TPV weather process. The simulation area is (95°–115°E, 25°–45°N), and the simulation period is from 1800 UTC 22 July to 0000 UTC 25 July 2010. The driving and boundary conditions of the numerical simulation are NCEP-FNL data with a time resolution of six hours, and the simulation area is in a single-layer nested form. We determined the specific parameterization schemes of the numerical simulation based on the reference and comparison of various parameterization schemes. The details are as follows:The horizontal resolution (time interval of output) is 3 km (1 hour), and the grid numbers (vertical layer numbers) is 1051 × 705 (51). Longwave and shortwave radiation transfer are represented by Rapid Radiative Transfer Model for Global Climate Models (RRTMG) scheme (Iacono et al., 2008). Other physics schemes employed in this study include a unified Noah land-surface model scheme (Chen et al., 1996b), Yonsei University (YSU) planetary boundary layer scheme (Hong et al., 2006), Morrison with aerosol scheme (Morrison et al., 2009), and Revised MM5 Monin-Obukhov scheme (Jiménez et al., 2012). Cumulus convective scheme is not considered here according to the research of Gao et al. (2018).

To verify the influence of SH from the surface of TP on the track and precipitation distribution of the TPV after it moved off the TP. The sensitivity experiment (Table 1) of ground SH is carried out by the WRF. The sensitivity scheme is used to test the influence of the surface SH on the track of the TPV and the distribution of precipitation by turning off the surface sensible heat flux over the TP.

3. 500-hPa temperature distribution over the ESTP

3.1. *Overview of the TPV*

According to the results given by MRD (Fig. 1), the TPV was generated at 0600 UTC 19 July 2010 over the Ngari Prefecture of Tibet. After its generation, it continued to move northeastward and moved off the TP at 0000 UTC 22 July. After moving off the TP, the TPV wandered to the east of the TP then moved slowly southward along the eastern edge of the TP, and existed over the ESTP for more than 60 hours. At 0000 UTC 25 July, the TPV rapidly moved southwestward, reentered the TP 12 hours later, and finally died out at 1800 UTC 25 July near the Nyingchi Prefecture, Tibet Autonomous Region. The track of the TPV determined by the TPV yearbook (figure omitted) was roughly consistent with the results given by MRD after 0000 UTC 21 July.

It can be seen from Fig. 1 that the TPV moved off the TP at 0000 UTC 22 July and remained over the ESTP for a long time, which is the special feature of the track of the TPV and an important reason for choosing this process as a

Table 1. Experiments designed for the ground sensible heat fluxes.

Experiments	Configuration of Numerical Model Parameters	Modification of ground sensible heat
Control Experiment (i.e., CNTR)	Same as the semi-ideal numerical simulation described in section 2.3	Use model-computed *u** and heat and moisture fluxes
Sensitivity Experiment (i.e., SENSI)	Same as the semi-ideal numerical simulation described in section 2.3	Use model-computed *u** and specified heat flux by tke_heat_flux

Note: *u** is the *U* momentum at the western and eastern boundary in the WRF.

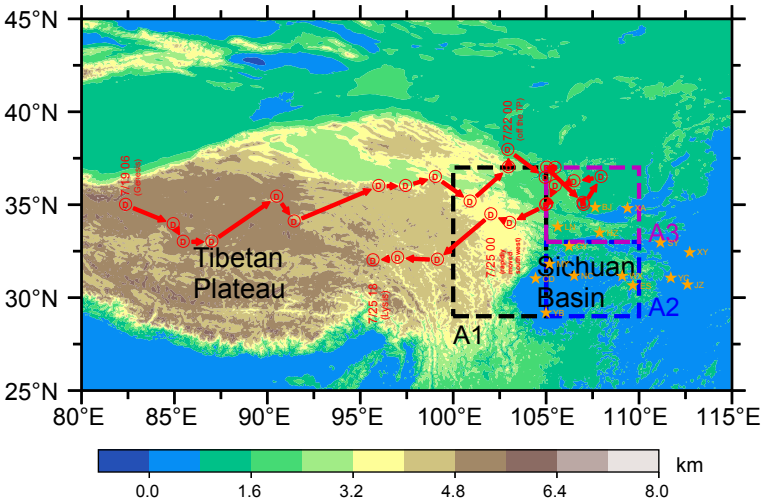

Fig. 1. The topographic features of the TP and its surroundings and the TPV track at 500-hPa from 0600 UTC 19 July to 1800 UTC 25 July at 6-h intervals. The locations of selected Doppler radar sites (YB, CD, NC, WX, MY, GY, HZ, LN, XA, BJ, SY, YC, JZ, XY) are marked by orange asterisks. The locations of AWS sites are too many (about 2500 sites) to be marked. The black, blue, and purple dotted boxes denote the A1, A2, and A3 regions, respectively. The "D" represents the TPV and the "D" in the circle represents the location of the TPV center.

typical case to study the influence of DH on the TPV. For the convenience of the study, we divided the main influence regions over the ESTP into three parts, including A1, A2, and A3 regions (Fig. 1). The A1 region is mainly a plateau region, The A2 region is mainly affected by the advection of DH related to plateau terrain, and the A3 region is the main activity area of the TPV center after the TPV moved off the TP. The three regions are 10° in longitude from east to west and 8° in latitude from north to south and slightly larger than the main circulation area of the TPV, which can roughly cover the active region of the TPV from 23–24 July 2010.

3.2. *Effects of TPV on the 500-hPa temperature distribution over the ESTP*

Although the average elevation of the A2 and A3 regions is significantly lower than that of the A1 region (Fig. 1), it can be seen from Fig. 2a that the time series of the 500-hPa temperature over the A1 region in July was highly correlated with that over A3 region ($r > 0.8$, $p < 0.01$), while the correlation of temperature between A2 region and A1 region was generally low. There are two main reasons for this phenomenon. 1) The A2 region is mainly located over the Sichuan Basin, and the lower elevation of the basin (500-hPa air is farther away from the underlying surface) causes the SH from the ground on air at 500-hPa to be weaker than that over the A1 and A3 regions. 2) The influence of the westerly wind from the TP is most obvious over the A3 region, and the temperature near the surface of the TP is relatively high, which makes the effect of temperature advection over the A3 region more significant (Fig. 2b). However, the A2 region is mainly affected by southerly airflow which does not pass through the TP, and the temperature along the route has a low correlation or even a negative correlation with the temperature over A1 region. Temperature advection also tends to reduce the correlation of temperature between the A1 and A2 regions. To sum up, differences in the SH transmitted from the ground caused by different underlying surface elevations, and differences in temperature advection caused by different wind directions result in differences in temperature trends over A1, A2, and A3 regions. As a result, the trend of temperature over A3 region is closer to A1 region than A2 region. However, it can be seen from Fig. 2c that the activity of the TPV over the ESTP forced the temperature over A2 region to be closer to A1 region. Based on the difference between the temperature distribution during 21–25 July 2010, the climate distribution characteristics, and the arc-shaped characteristics of temperature distribution during the period of the TPV occurrence (Fig. 2c), we are more inclined to believe that the circulation of the TPV first and actively affected the distribution of temperature over the related regions. In the next section, we will analyze in detail how the TPV changed the climate characteristics of temperature distribution over the ESTP and resulted in the abnormal warming of 500-hPa air over the A2 region and how the change in the temperature distribution affected the distribution of the TPV-associated precipitation and the track of the TPV.

4. Influence of DH associated with TP terrain on the development of the TPV

4.1. *Relationship between TPV circulation and DH associated with the TP*

From 23–24 July 2010, the 500-hPa temperature over

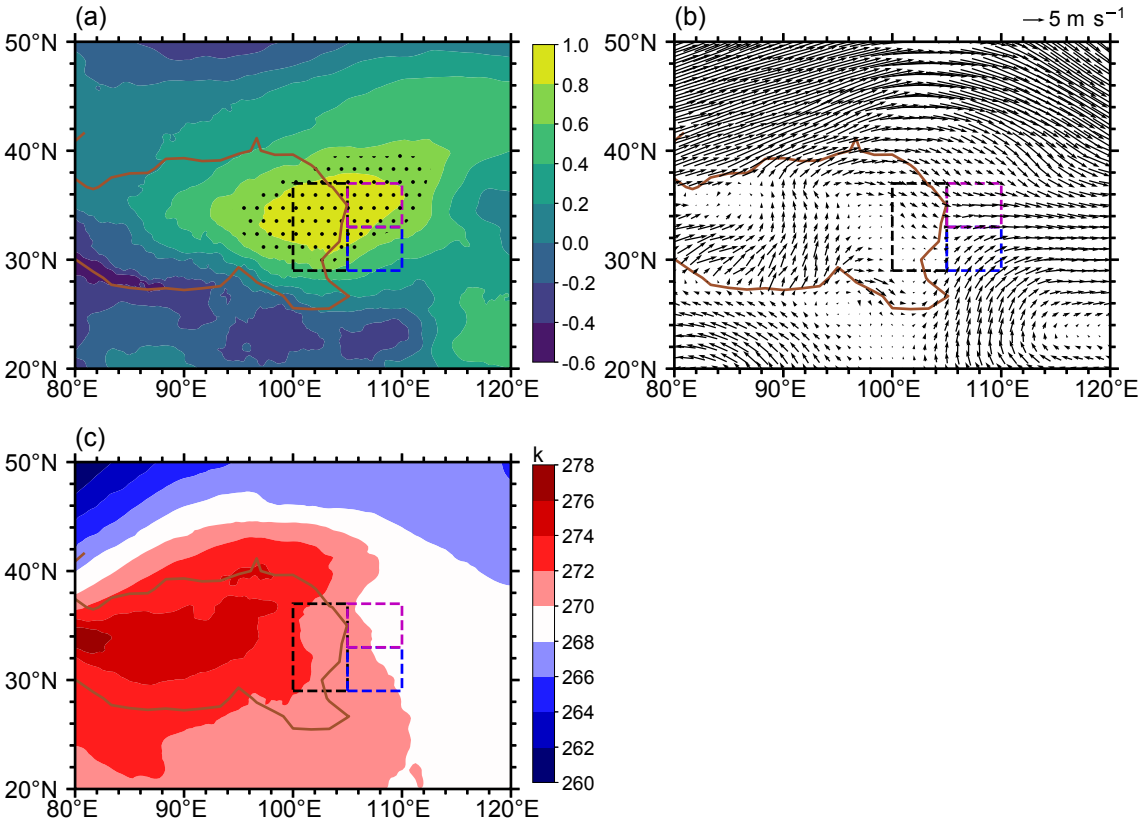

Fig. 2. (a) Correlation coefficient between the area-averaged 500-hPa temperature over the A1 region and temperature over the TP and its surrounding areas during 1–31 July 2010. Dots in (a) indicate statistically significant areas where the correlation coefficient is greater than 0.6 ($p < 0.01$, using a two-tailed t-test). (b) the 500-hPa wind field averaged over 1–31 July 2010. (c) the 500-hPa temperature averaged over 21–25 July 2010. The topographic height thresholds corresponding to 3 km above mean sea level (brown line) are shown.

the A1 region was 2–4 K higher than that over A2 and A3 regions (Fig. 3). At 0000 UTC 23 July 2010, the A1 region was mainly affected by the northward wind to the west side of the TPV center, and most of the area was controlled by strong warm advection. The northerly wind to the west of the TPV center was mainly distributed over the east side of the TP (near 105°E), and gradually turned to the southwest wind due to cyclonic shear near 30°N. The southwesterly wind with speeds exceeding 10 m s^{-1} almost vertically crossed the 270 K isotherm over the A2 region, causing the A2 region also to be affected by strong warm advection. However, the angle between the southerly wind and isotherms became smaller, which made the wind less able to transmit the temperature differences over the A3 region, thus the A3 region was less affected by warm advection (Fig. 3a). It should be noted that there was a strong southeast wind to the south of the A2 region; the subsequent cold advection and the cold advection caused by the southwest wind converged over A2 region, thus weakening the strength of the warm advection over A2 region. This was also the main reason why the advection transport intensity of the DH over the A1 region was significantly higher than that over the A2 region during this period (Fig. 4c).

At 1200 UTC 23 July 2010, as the position of the TPV moved eastward, the northerly wind on the western side of the TPV center became less influenced by the TP, and the northeasterly wind prevailed over more than half of the A1 region, resulting in a significantly weaker warm advection intensity over the A1 region. However, the northerly wind on the western side of the TPV center passing over the TP continued to affect the A2 and A3 regions. As a result, the A2 and A3 regions were still affected by strong warm advection (Fig. 3b). This was also the reason why the advection transport of DH over the A2 and A3 regions had remained positive during this period.

At 0000 UTC 24 July 2010, with the southward development of the TPV, the TPV center was close to the TP again, and the strong warm advection over the A1 region was restored. The difference was that the intensity of the southerly airflow to the south of the A2 region weakened and its position was further east, so the influence of the cold advection caused by it over the A2 region was constantly weakened. Therefore, the advection transport effect of DH over the A2 region was significantly improved during this period. Under the influence of the airflow near the TPV center, the wind directions were different over the A3 region, which gradually weakened the average temperature advection intensity over this region (Fig. 3c).

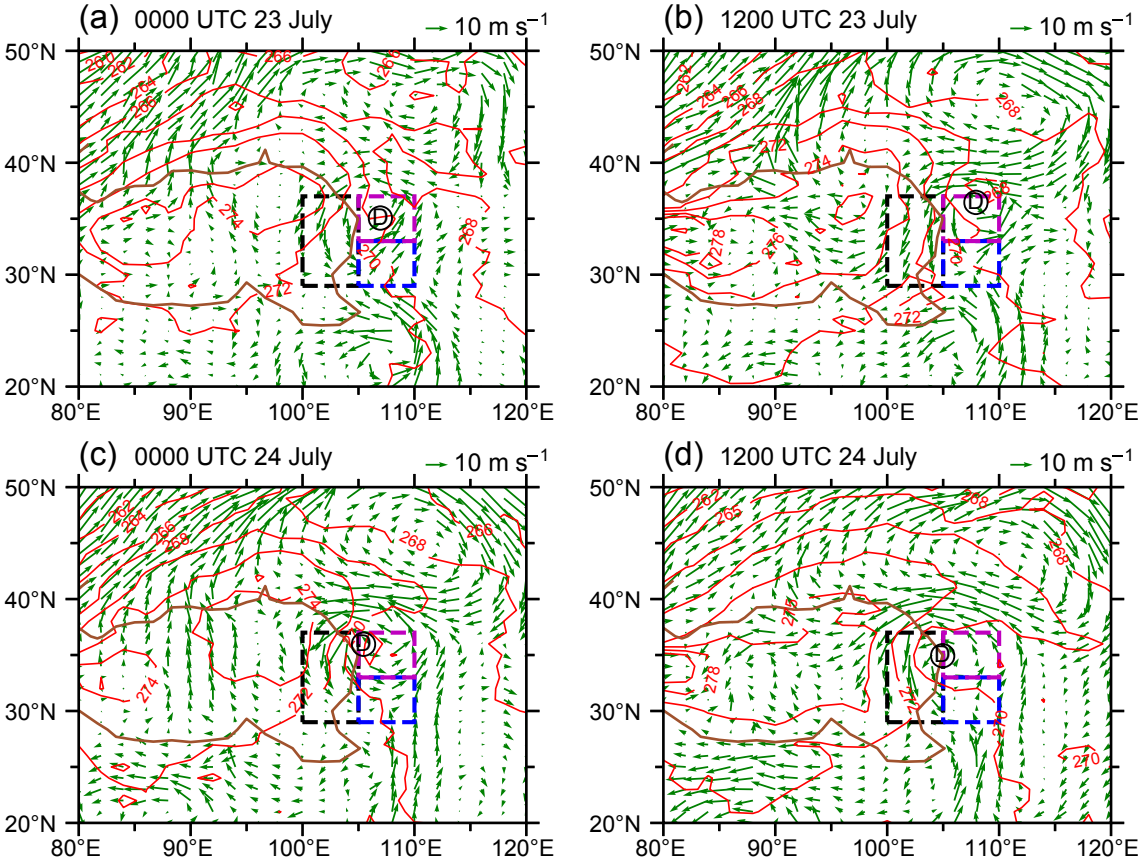

Fig. 3. (a–d) Horizontal winds (vectors) and 500-hPa temperature (K; red contours) from 0000 UTC 23 July to 1200 UTC 24 July 2010 at 12-h intervals. The black, blue, and purple dotted boxes denote the A1, A2, and A3 regions respectively. The topographic height threshold (brown line) corresponding to 3 km above mean sea level is shown. The "D" represents the TPV and the "D" in the circle represents the location of the TPV center.

At 1200 UTC 24 July 2010, as the TPV moved further towards the main body of the TP, the northerly wind to the west side of the TPV center gradually blew from colder to warmer areas over the A1 region, and the warm advection over the A1 region significantly weakened and gradually turned into cold advection, and the northerly wind passing over the TP significantly weakened when it passed over A2 region (Fig. 3d). At this point, the warm advection caused by the circulation of the TPV gradually disappeared over the three regions.

To further study the influence of DH on the three regions at 500-hPa, the Q_t, Q_h, and Q_v over the three regions were analyzed independently.

As shown in Fig. 4a, the high correlation between the 500-hPa temperature over the A1 and A3 regions was further verified by the time series of the average regional temperature. The average temperature over the A1 region was usually 1–3 K higher than that over A2 and A3 regions, and the time series of average temperature over the A1 and A3 regions presented obvious and consistent diurnal variation characteristics. The highest intra-day temperature over the two regions usually occurred around 1200 UTC, while the lowest temperature usually occurred between 0000 and 0600 UTC. The 500-hPa temperature over the A2 region also had certain diurnally varying characteristics, but it was not consistent with the diurnal variation of temperature over the A1 and A3 regions. Before 25 July, the average 500-hPa temperature over the A2 region was always at the lowest level among the three regions. It is worth noting that the temperature difference between the A1 region and the A2 and A3 regions gradually increased with the eastward development of the TPV, and the temperature difference between the A1 and A2 region reached its maximum during 0000–0600 UTC 24 July which played a key role in strengthening the effect of DH advection. During this period, the TPV center moved slowly to the east of 105°E, and the double-arc precipitation region was not yet obvious.

DH has a very important effect on temperature change. The local change of DH (LCDH) is mainly affected by Q_t, Q_h, and Q_v. The LCDH was relatively complicated because it was affected by many factors such as shortwave radiation, sky conditions, surface sensible heating, and water vapor phase transformation. However, the local change in the magnitude and trend of DH over the three regions were relatively consistent. The LCDH over the A1 region was greater than that over the A2 and A3 regions before the TPV moved off the TP and at the initial stage of the TPV moving out of the TP. As the TPV moved off the TP and gradually moved south-

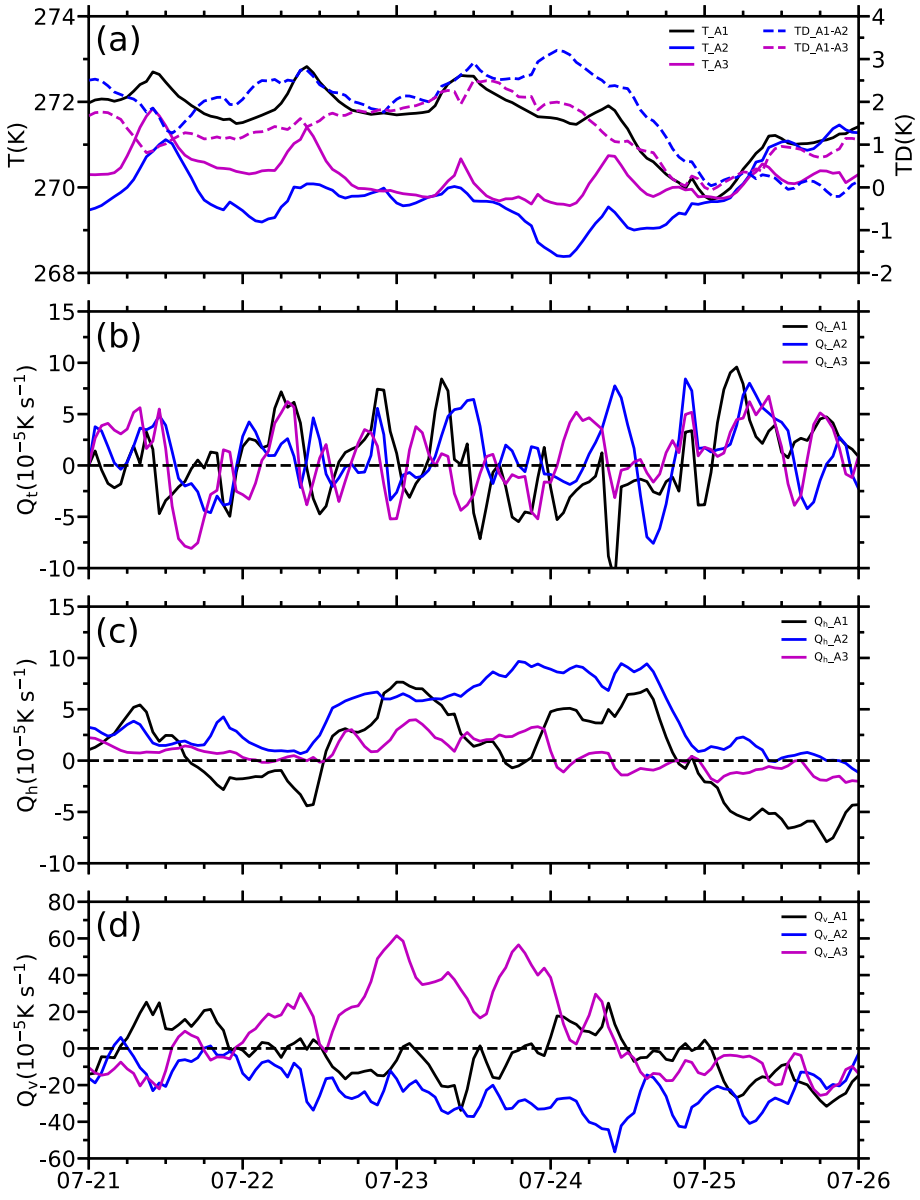

Fig. 4. (a) Time series of the area-averaged 500-hPa temperature (T) and area-averaged 500-hPa temperature difference (TD) between the A1 region and A2 and A3 regions. (b) Time series of the area-averaged 500-hPa Q_t over A1, A2, and A3 regions. (c–d) As in (b), but for Q_h and Q_v.

ward, the LCDH over the A2 and A3 regions was significantly higher than that over the A1 region (Fig. 4b).

The DH advective transport over the A2 and A3 regions became particularly obvious when the TPV moved off the TP. The increase in the temperature difference between different regions was the basic condition supporting the increase in the advective transport of temperature. By comparing Figs. 4a and 4c, it can be seen that the increase of DH advective transport over the A2 and A3 regions was consistent with the increased temperature difference between the two regions and the A1 region. Under the continuous influence of the westerly airflow to the south of the TPV center, the strong DH advection over the A2 region persisted from 1200 UTC 22 July to 1800 UTC 24 July. During this period, the TPV developed to the east of the main body of the TP. The north wind to the west of the TPV center continues to affect the A1 region which gradually changes downstream to a west wind on the south side of the TPV center, thus affecting the A2 region, which has the effect of further strengthening the DH advection over the A2 region (Fig. 4c). The DH advective transport over A3 region was positive from 1200 UTC 22 July to 0000 UTC 24 July, and decreased to near zero after 0000 UTC 24 July. During this period, the difference in DH advective transport over the A2 and A3 regions was mainly due to the southward movement of the TPV center, and the subsequent change in wind velocity made it difficult for the DH over the A1 region to be transported to A3 region through advection.

From 1200 UTC 22 July to 1200 UTC 24 July, the TPV center was mainly active over the A3 region. The strong upward movement near the TPV center resulted in extremely strong Q_v in this region, with a maximum value exceeding 0.0006 K s^{-1} (Fig. 4d). In the same period, Q_v over the A2 region had always been negative, which indicated that the increasingly positive contribution of temperature over the A2 region mainly came from Q_h. Q_v over the A1 region had certain diurnally varying characteristics, especially during 23–24 July. Positive values of Q_v mainly appeared in the daytime.

It is worth mentioning that there was a certain correlation between Q_h and Q_v over the A1 region. The positive period of Q_v usually corresponded to the positive period of Q_h, particularly on 24 July. The bimodal structure of Q_v over region A1 corresponded well to Q_h, and time trend of Q_v preceded that of Q_h . It can be seen from (Fig. 7d) that the A1 region was not the main region of the precipitation, which indicates that water vapor condensation was not the main source of DH, and the following analysis will show that the vertical transport of SH from the TP terrain during this period could be considered as an important reason for the atmospheric warming at 500-hPa over the A1 region.

In conclusion, due to the large temperature difference between the A1 region and the A2 and A3 regions, and the continuous influence of the westerly flow after the southward movement of the TPV, the influence of Q_h over the A2 region was significantly higher than that over the A3 region. As a result, the 500-hPa temperature over the A2 region continued to rise from 0000 UTC 24 July. By 0000 UTC 25 July, the 500-hPa temperature over the A2 region tended to be consistent with that over the A1 region (Fig. 4a). It will be discussed in detail below that the atmospheric warming at 500-hPa over the A2 region is caused by Q_h associated with the plateau terrain and was the key factor affecting the TPV-associated precipitation and the track of the TPV.

4.2. *Influence of the advection of DH on TPV-associated precipitation*

SH and LH are considered to be the two main forms of DH. To further confirm the distribution characteristics of SH and LH in the three regions and reveal the mechanism of SH and LH on the development of the TPV as it moved off the TP, the DH rate and drying rate over the three regions were calculated from 0000 UTC 21 July to 0000 UTC 26 July. The DH rate represents the overall level of DH in a region, while the drying rate represents the contribution of condensation heat release of water vapor to the DH of the atmosphere. It can be seen from Fig. 5 that the DH rate and drying rate over the three regions were significantly different. As the A1 region was located over the TP and the 500-hPa atmosphere was close to the underlying surface, its DH rate and drying rate showed certain diurnally varying characteristics. For example, the positive value of the DH rate often appeared in the daytime. Due to solar radiation, the surface temperature of the TP rose rapidly in the daytime, which easily led to the rapid warming of the air above the TP. At the same time, higher temperatures easily caused the evaporation of water vapor, and the heat absorption effect of the evaporation process led to a negative drying rate. As can be seen from Fig. 5a, at 0000 UTC 24 July, before the temperature of the A2 region kept rising due to strong warm advection, the DH rate over the A1 region was positive (~1 K d^{-1}) and showed a rapidly rising trend. By 0600 UTC 24 July, the DH rate over the A1 region had risen to about 2 K d^{-1}. Over the next 12 hours, the DH over the A1 region remained in the positive range. It is worth noting that the drying rate over the A1 region during this period was always negative, indicating that the heat source of DH advection over the A1 and A2 regions mainly came from the SH related to the surface of the TP (A1 region). It was the heating of the atmosphere above the plateau topography over the A1 region that created the prerequisite for the apparent temperature advection over the A1 and A2 regions. It is particularly noteworthy to point out that this period (from 1200 UTC 23 July to 0000 UTC 25 July) happened to correspond to the period when the double-arc precipitation area gradually formed as the TPV center moved westward.

The 500-hPa atmosphere over the A2 region was far away from the underlying surface, so the DH rate was mainly negative. In addition, it was the main region where the TPV-associated precipitation occurred. As shown in Fig. 5b, the drying rate had been significantly positive due to water vapor condensation. It is worth mentioning that since 0600 UTC 24 July, the DH rate over the A2 region slowly increased, while the drying rate gradually decreased, which suggests that the warm advection of DH could slow down the downward trend of DH and limit the heat release process due to condensation of water vapor, thus reducing the drying rate over A2 region. The possible mechanism of the DH advection limiting precipitation intensity in the A2 region will be specifically revealed below.

In contrast to the A2 region, the A3 region was mainly characterized by a positive DH rate and negative drying rate before 0600 UTC 24 July. This might be related to the vertical transport of DH caused by strong upward movement near the TPV center over the A3 region. After 0600 UTC 24 July, as the TPV center was closer to the Sichuan Basin, abundant water vapor combined with strong upward motion led to obvious precipitation near the TPV center, and the numerical characteristics of the DH rate and drying rate gradually became consistent within the A2 region (Fig. 5c).

As can be seen from the above analysis, the effect of SH related to the TP topography on the 500-hPa atmosphere led to the high temperatures at 500-hPa over A1 region, and then the high temperature over the A1 region was transferred to the A2 region through advection, so that the temperature over the A2 region kept rising. Therefore, to realize the atmospheric warming at 500-hPa over the A2 region, two conditions needed to be met. 1) Due to the SH effect related to the TP topography, the 500-hPa temperature over the A1 region was higher than that over the A2 region. 2) The wind field of the TPV conveyed the high-temperature air over the

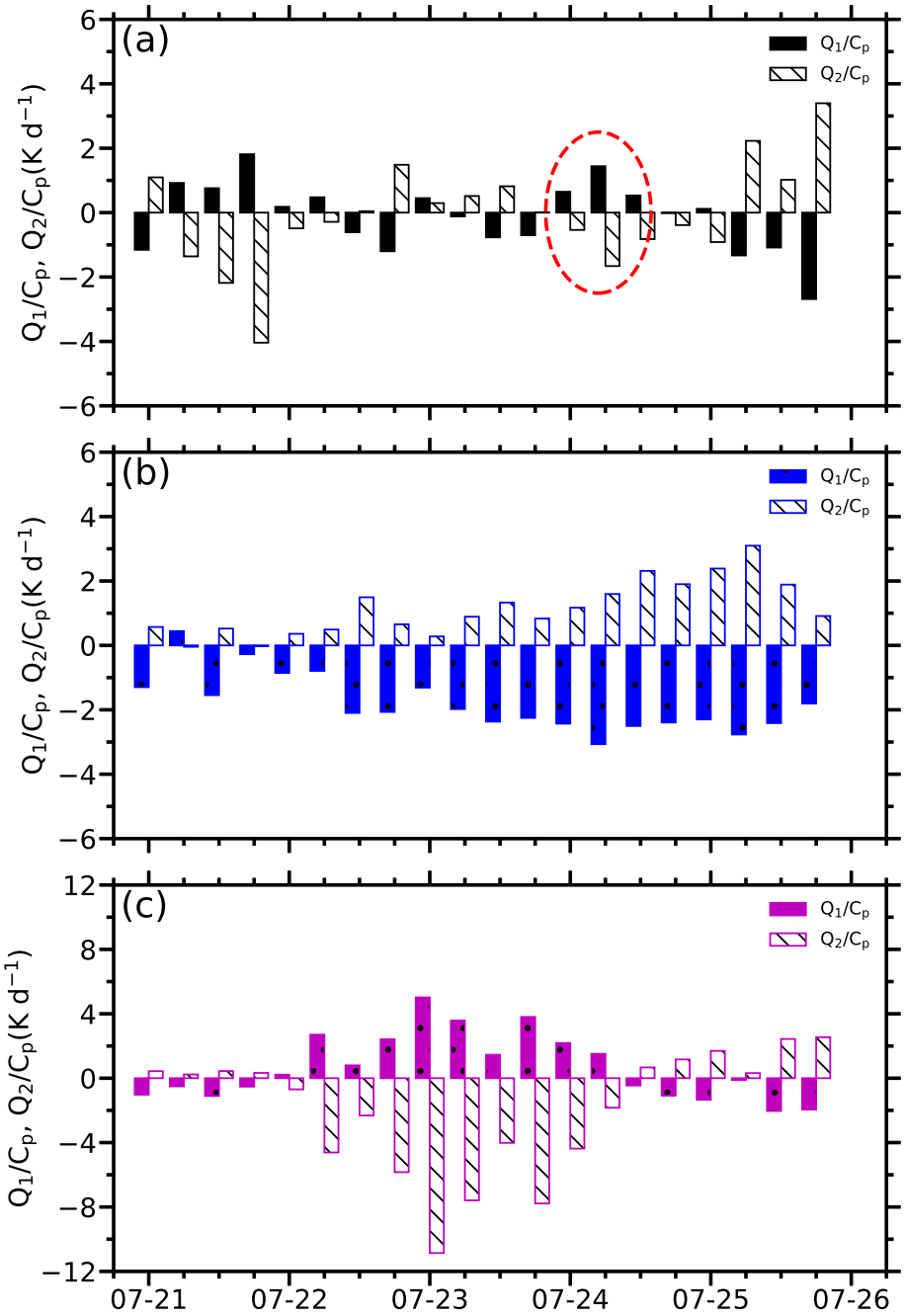

Fig. 5. (a) Time series of area-averaged 500-hPa DH rate (Q_1/C_p) and drying rate (Q_2/C_p) over the A1 region during 21–26 July. (b)-(c) Same as in (a), but for the A2 and A3 regions. The red dashed ellipse in (a) shows the obvious period of SH over the A1 region.

TP (A1 region) to the A2 region through advection. This was also the main reason why the activities of the TPV mentioned above could change the atmospheric temperature and climate distribution characteristics at 500-hPa over the ESTP and formed the temperature distribution characteristics as shown in Fig. 2c.

As shown in Fig. 6a, under the continuous influence of warm advection, the temperature of the atmosphere to the east and south of the TP center at 500-hPa was significantly higher than that of the surrounding area, forming an obvious warm cover. At the same time, due to the low humidity of the air passing over the TP, the dry advection formed an arc-shaped banded dry area in the circulation at a height of about 500-hPa to the south of the TPV center, which manifests itself as a symmetric area of a negative humidity anomaly to the east and west sides of the TPV center on the vertical profile of humidity anomaly (Fig. 6b). The dry and warm layer (band) located at about 500-hPa inhibited the development of convection below 500-hPa.

Under the influence of continuous warm advection, the arc-shaped dry and warm layer (band) at 500-hPa became particularly obvious around 1200 UTC 24 July. As can be seen

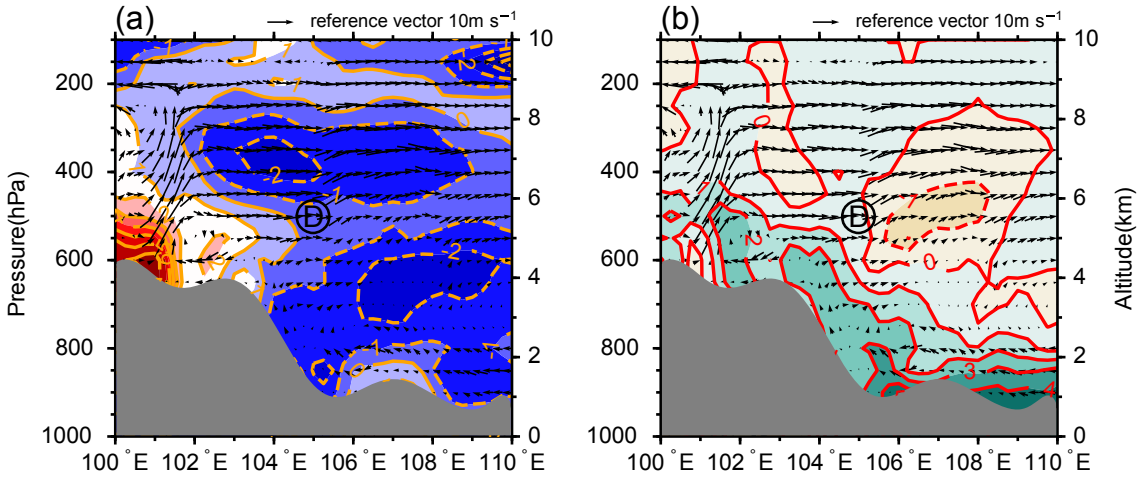

Fig. 6. (a) Vertical cross-section of the temperature spatial anomalies (K) along 32.5°N at 1100 UTC 24 July 2010. (b) As in (a), but for the specific humidity spatial anomalies (g kg^{-1}). The "D" represents the TPV and the "D" in the circle represents the location of the TPV center.

from Fig. 7b, the warm advection was the most powerful over the A1 region to the west of the TPV center. Accompanied by the cyclonic circulation of the TPV, the strong warm advection could affect the southern and eastern sectors of the TPV circulation, presenting an obvious arc-shaped zonal distribution characteristic, which was consistent with the dry and warm layer (band) at 500-hPa. It can be seen from Fig. 7a that the dry and warm layer (band) significantly inhibited convective development in the region where it was located. The TBB of the cloud top over the relevant region was generally higher than 280 K (the height of cloud top development was low), indicating that it was an area with little or no rain. The TBB of the cloud top was generally lower than 210 K over the inner part of the arc region close to the TPV center and the outer part far from the TPV center, indicating that these two regions had strong convection and high cloud top height development (rainfall areas). Based on Figs. 7c and 7d, it can be seen that the distribution of precipitation particles in the atmosphere and precipitation area on the ground during this period presented a double-arc distribution, with the TPV center at its focal point. The dry and warm layer (band) cut the whole precipitation area originally distributed along the southeast side of the TPV center into two arc-shaped heavy precipitation areas, and between the two precipitation areas was an area of clear sky with little rain (Fig. 7d).

4.3. *Influence of DH along the track of the TPV*

The above analysis has proven that the SH from the surface of TP can affect the TPV-associated precipitation area, and it is pointed out that Q_h was the important factor in forming the double-arc precipitation area associated with the TPV. However, the LH related to precipitation would become the dominant factor affecting the development of the TPV after it moved off the TP (Dong and Li, 2015). Therefore, to understand how the SH from the surface of TP affected the development of the TPV that moved off the TP, the possible relationship between LH and the intensity and the track of the TPV should be clarified first.

According to the research of Wang et al. (1993), the local change of potential vorticity (LCPV) caused by DH can be described by the formula as follows:

$$\frac{\mathrm{d}(\mathrm{PV})}{\mathrm{d}t} \approx -g(f+\zeta)\frac{\partial \dot{\theta}}{\partial p}, \tag{4}$$

where $\dot{\theta} = \mathrm{d}\theta/\mathrm{d}t$, which can measure the change in DH. θ is the potential temperature, f is the Coriolis parameter, ζ is the absolute vorticity, and g is the acceleration of gravity.

According to the relationship between DH and LCPV described by Eq. (4), it can be seen that the equipotential temperature surface will move closer to the LCPV maximum value center in the vertical direction, resulting in a larger vertical distance between the isentropic surface above and below the large value center of PV (Shou, 2010). According to the conservation principle of PV (Hoskins et al., 1985), the cyclonic vorticity of the air column will increase with increasing distance between isentropic surfaces, which is conducive to the strengthening of the TPV. Considering that LH is the major component of DH generated by precipitation, the above mechanism completely explains how LH affects the intensity of the TPV. In addition, we believe that the LH could guide the track of the TPV by strengthening its circulation asymmetrically.

Figure 8 shows the distribution characteristics of precipitation, the LH, and the LCPV in the development area of the TPV from 1200 UTC 23 July to 2400 UTC 24 July. This is the key period for the formation of a double arc-shaped precipitation area and the east-to-west track of the TPV.

During the period from when the TPV moved off the TP until 2400 UTC 23 July, the TPV-associated precipitation was mainly concentrated on the southeast side of the TPV center (figure not shown). The zonal distribution of the average precipitation presented a unimodal structure and the maximum value of the precipitation appeared near 110°E (Fig. 8a). Corresponding regions with large values of DH

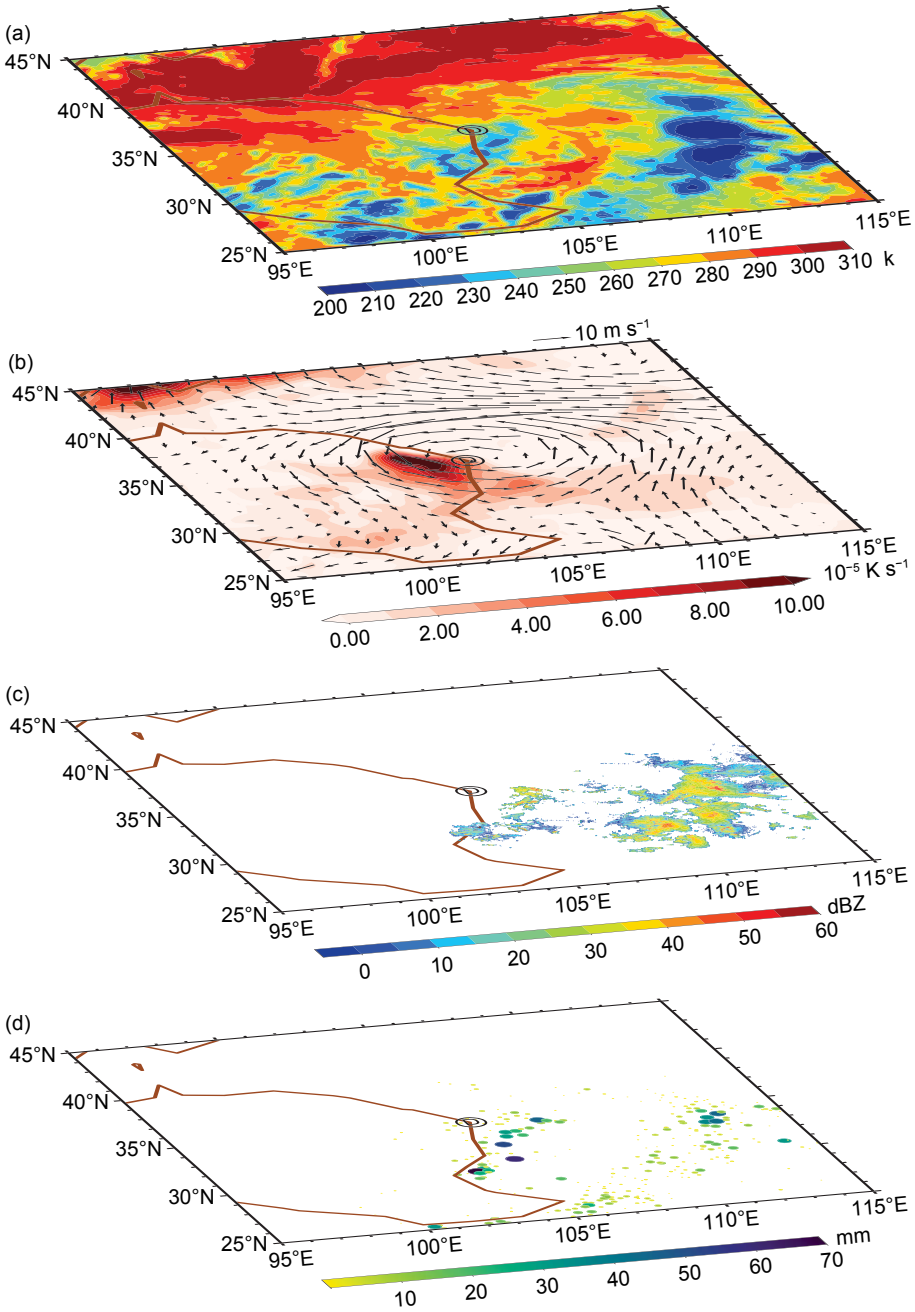

Fig. 7. (a) Horizontal distribution of the TBB (K), (b) the 500-hPa temperature advection, and (c) the RMCR over the ESTP at 1200 UTC 24 July 2010. (d) Horizontal distribution of the accumulated precipitation observed by the AWS in the ESTP domain from 1200–1500 UTC on 24 July (3 h). The topographic height thresholds of 3 km above mean sea level (brown line) are shown. The "D" represents the TPV and the "D" in the circle represents the location of the TPV center.

were mainly concentrated in the region between 107°–113°E (Fig. 8b). Based on the distribution of the positive center of LCPV and the position of the TPV center (~107°E) in this period, it can be seen that the LH released by precipitation could still support the eastward development of the TPV (LCPV increased obviously to the east side of the TPV center). However, from 0000 to 1200 UTC on 24 July, a bimodal structure of precipitation gradually formed (Fig. 8a), and the corresponding large value area of DH was divided into two parts just like the precipitation areas. An obvious low-value area of DH appeared over 107°–112°E (Fig. 8c). It is worth noting that both the large value region of DH and the area of increasing LCPV are concentrated near 105°E, while the TPV center was still in the east region of 105°E in this period. Therefore, the increasing LCPV in this period would mainly strengthen the circulation to the

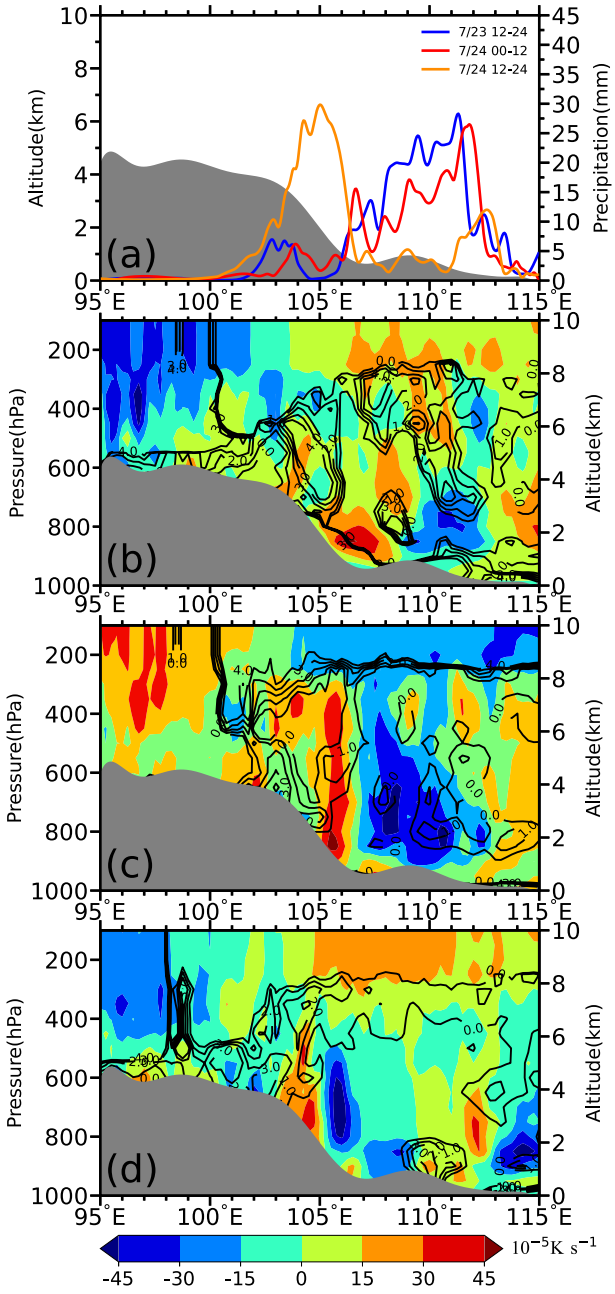

Fig. 8. (a) Area-averaged accumulated precipitation in 12 h observed by AWS between 29° and 37°N. Vertical cross-section of the area-averaged 12-h mean DH rate (10^{-5} K s^{-1}; color shading) and the 12-h local change of area-averaged PV (PVU; contours) between 29° and 37°N during (b) 1200–2400 UTC 23 July, (c) 0000–1200 UTC 24 July, and (d) 1200–2400 UTC 24 July. The gray shading indicates the area-averaged topography of the ESTP between 29° and 37°N.

west side of the TPV center. The asymmetric strengthening for the TPV was very helpful to guide its westward development. From 1200 to 2400 UTC 24 July, with the further formation of the double arc-shaped precipitation area, the bimodal characteristics of the zonal distribution of precipitation became more obvious (Fig. 8a). The continuously enhanced LCPV in the region west of 105°E would continue to strengthen the circulation to the west side of the TPV center (Fig. 8d), thus further guiding the TPV to develop westward.

Both the above analysis and existing studies have pointed out that PV is a good indicator of the development and movement direction of TPVs (Li et al., 2011, 2014, 2019). Figure 9 also intuitively shows the high correlation between the large value of PV and the track of the TPV. As shown in Fig. 9, there was an obvious large-value center of PV to the east side of the TPV center at 0000 UTC 21 July. Until 0000 UTC 23 July, there was a large value distribution area in front of the easterly path of the TPV at 500-hPa. As mentioned above, the growth of PV was closely related to the LH at 500-hPa. This corresponded to the period when the track of the TPV turned from eastward to westward and the TPV-associated precipitation was the strongest from 0000 UTC 23 July to 0000 UTC 25 July. At 1200 UTC 23 July, the PV to the east side of the TPV center was generally less than 0.7 PVU, while the PV to the west side of the TPV center was significantly larger than that on the east side contemporaneously, and its value was generally greater than 1 PVU. This could explain why the TPV did not continue to develop as it moved eastward. The phenomenon that the track of the TPV was consistent with the large-value region of PV was most obvious from 23 to 24 July (Fig. 9).

Although PV serves as a good indicator for the movement of the TPV, we need to clarify that the TPV-associated precipitation was the root cause of the LCPV. The reason why PV can guide the movement direction of the TPV is not only due to the increase in its value, but even more importantly the characteristics of its location and distribution characteristics. It was the formation of the double arc-shaped precipitation area that led to the increase of PV over the inner arc-shaped precipitation area, and the rain-free area between the two arc-shaped precipitation areas hindered any further eastward development of the TPV. Therefore, it is not so much that the PV offers a better indication for the movement of the TPV, rather the TPV-associated precipitation serves as a better indicator for the movement of the TPV. This begs the question, what is the factor which contributed to the formation of the double arc-shaped precipitation area? The answer is SH from the surface of the TP.

To prove that the SH from the ground of the TP influenced the TPV-associated precipitation distribution and the track of the TPV, we applied the WRF to carry out SENSI designed in section 2.3 on SH from the TP surface. According to the simulation results of the CNTR (Figs. 10a–d), under the condition that the TP surface sensible heat flux was not turned off, the location of the TPV center and the double-arc precipitation distribution were consistent with that from the ERA5 data and the observation results, which indicated that the CNTR successfully simulated the track of the TPV and the characteristics of the precipitation area during this period.

According to the above analysis, the warm cover formed by the SH from the TP ground at 500-hPa was the main reason for the formation of the precipitation distribution. By comparing Figs. 10a and 10e, it could be seen that

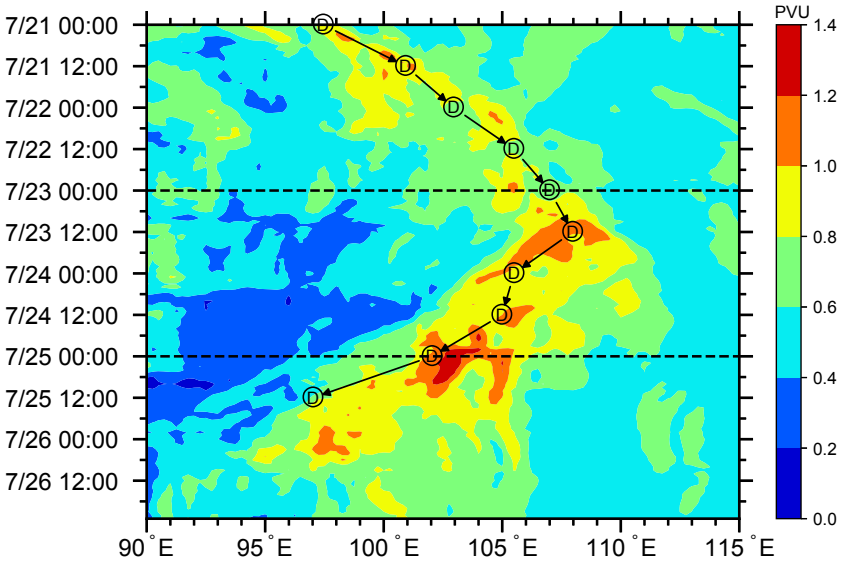

Fig. 9. Temporal variation of PV (units: PVU, 1 PVU=10^{-6} K m^2 kg^{-1} s^{-1}) at 500-hPa and the longitude position of the TPV center from 0000 UTC 21 July to 1200 UTC on 25 July at 12-h intervals. The two black dotted lines indicate the time of 0000 UTC 23 July and 0000 UTC 25 July. The "D" represents the TPV and the "D" in the circle represents the location of the TPV center.

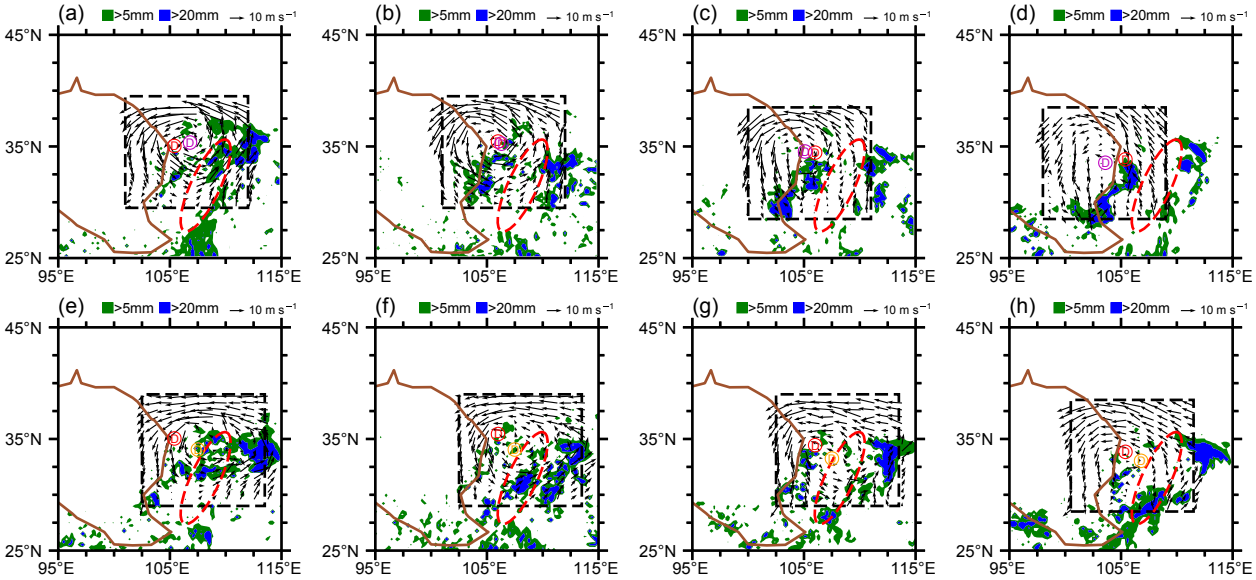

Fig. 10. The accumulated precipitation in the next 6 hours overlaid with 500-hPa winds near the TPV center from the (a–d) CNTR and (e–h) SENSI using the WRF from 0000 UTC 24 July to 0000 UTC 25 July 2010 at 6-h intervals. The "D" represents the TPV and the red, purple, and yellow "D" in the circle are the locations of the TPV center obtained from MRD, CNTR, and SENSI results, respectively. The red dashed ellipse is the location of the rain-free area between the two arc-shaped precipitation areas based on the data observed by AWS. The topographic height threshold of 3 km above mean sea level (brown line) is shown.

at 0000 UTC 24 July 2010, there was little difference in the precipitation area simulated by the CNTR and SENSI. The TPV-associated precipitation was mainly distributed east of the TPV center. However, the location of the TPV was significantly further east in the SENSI. By 0600 UTC 24 July 2010, the precipitation area associated with TPV simulated by the CNTR and SENSI began to show obvious differences. The precipitation area in the SENSI did not show the double-arc distribution characteristics and large precipitation was simulated in the area that should have no rain (Fig. 10f). Based on the results of the above analysis regarding LH and TPV development, it can be seen that such differences in the precipitation distribution would make it easier for the TPV in the SENSI to develop eastward. The results also

proved that the position of the TPV continued to move east to near 107°E due to the LH caused by precipitation on its east side in the simulation results of SENSI at 1200 UTC 24 July 2010 (Fig. 10g). However, in the CNTR, due to the barrier of the rain-free area between the two arc-shaped precipitation areas, the center of the TPV moved westward to the vicinity of 105°E (Fig. 10c). At 1800 UTC 24 July 2010, according to the results of CNTR, the double-arc distribution characteristics of the TPV-associated precipitation were the most obvious, and the TPV center also moved westward to the TP region (Fig. 10d). On the other hand, the results of SENSI at the same time showed that the TPV-associated precipitation did not form an obvious double-arc distribution characteristic, and the location of TPV center remained near 107°E (Fig. 10h).

By comparing the results of SENSI and CNTR, if the sensible heat flux from the plateau surface was turned off, it was difficult to form the double-arc precipitation distribution characteristics consistent with the observed results and the location of the TPV center would always develop to the east of the main body of the TP. This proved that SH from the TP surface could indeed affect the track of the TPV by affecting the distribution of TPV-associated precipitation after the TPV moved off the TP.

Through the above analysis and proof, we find that SH and LH run through the whole development process of the TPV, and their effects on the TPV are distinguishable and closely related, which is a synergistic relationship. The primary mechanisms are summarized in the schematic diagram of Fig. 11**.** We could separate the roles of SH and LH in the development of the TPV mainly from the object and effect. When the TPV moves off the main body of the TP, the SH from the TP surface will heat the specific area of the TPV circulation through advection, which inhibits the development of convection and then changes the distribution of the TPV-associated precipitation. LH can directly promote the strengthening of the TPV and is a significant indicator for the TPV track. It is particularly noteworthy that the LH is highly correlated with the precipitation process, so the active area of LH is also controlled by SH from the TP topography to a certain extent. At the same time, LH influences the intensity of SH advection by guiding the track (affecting the distance between the TPV and the main body of the TP) of the TPV.

5. Conclusions and discussion

The huge elevation difference, combined with the abrupt change of the surface SH, makes the ESTP the most critical area for the development of TPVs. However, most of the TPVs die out over the main body of the TP. Still, a few of the eastward-moving TPVs have a short residence time over the ESTP, which leads to limited research on the development of TPVs over the ESTP. In this paper, a TPV developed over the ESTP during 22–25 July 2010 was analyzed from the perspective of the influence of the DH based on ERA5 reanalysis data, RMCR data, FY-2E satellite data, and the precipitation data observed by AWS. The main conclusions are as follows.

(1) The huge elevation difference between the east and west sides of the ESTP results in a significant difference in SH on the east and west sides of the TPV. The circulation field to the west of the TPV center was obviously affected by SH due to the TPV circulation near the ground. Strong SH not only increased the local temperature but also

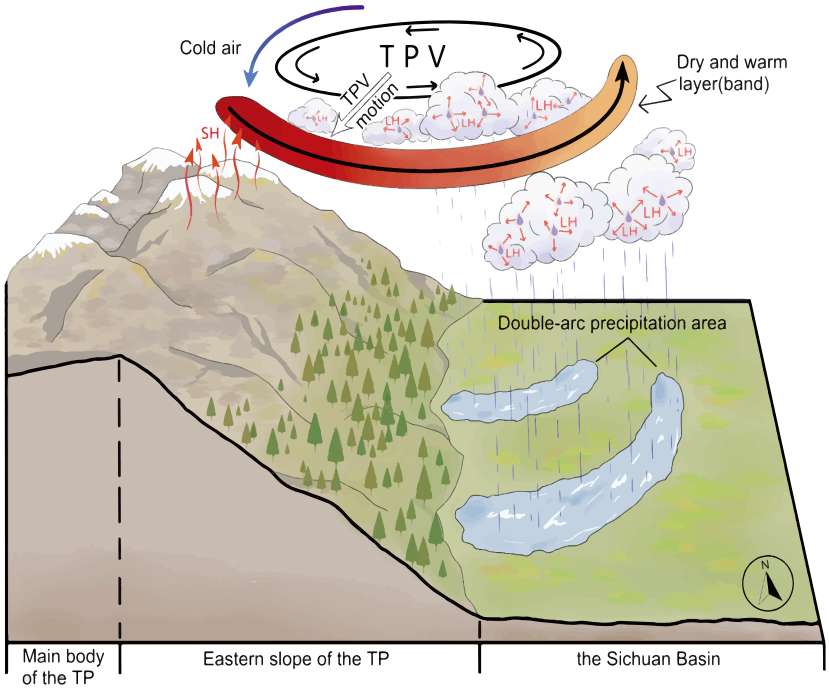

Fig. 11. Schematic diagram illustrating the effects of SH and LH on the precipitation distribution and the track of the TPV.

affected the atmospheric temperature of the southern or eastern circulation of the TPV with the help of the TPV circulation, which changed the thermal structure of the TPV circulation over the TPV-associated precipitation region.

(2) The DH advection combined with the TPV circulation could change the thermal structure of the TPV and lead to the formation of an obvious arc-shaped dry and warm layer (band) near 500-hPa. This dry and warm layer (band) serves to inhibit the development of convection, thus limiting the precipitation in the related region, so that the precipitation area originally distributed along the southeast side of the TPV was divided into a double arc-shaped precipitation area.

(3) Because of the double arc-shaped precipitation area, the strong LH generated by precipitation in the circulation of the TPV could only be distributed in the inner arc-shaped precipitation area closer to the TPV center and the outer arc-shaped precipitation area far away from the TPV center, and there was a large region without rain between the two arc-shaped precipitation areas. Due to the lack of LH released from water vapor condensation over the rain-free area, it was not conducive to the strengthening of PV, thus restricting the development of the TPV to the southeast direction. Over the inner arc-shaped precipitation area, the strong LH release (around the 500-hPa level) resulted in the strengthening of PV to the southwest side of the TPV center, which made the TPV develop southwestward.

In this case, however, the TPV was located over the ESTP for a long time, which provided the opportunity to study the influence of the TP on the TPV. In general, the TPV either disappeared rapidly or moved to a region far from the TP during a short time when it moved off the TP. Therefore, the governing processes based on this individual case may not apply to all TPV-associated weather processes.

There are many factors affecting the track of TPVs, and the strengthening of PV caused by LH is only one of them. In addition, the 200-hPa westerly jet and the 500-hPa trough or shear line often represent the large-scale conditions promoting the eastward movement of TPVs (Yu et al., 2007), and the background wind field in the active region of TPVs can also affect the movement direction of TPVs (Lin et al., 2020). Li et al. (2019) pointed out that the convergence between the northwest wind and southwest wind benefits the eastward movement and development of the TPVs, and found that the dynamic effects were more important than the thermodynamic effects.

Figure 12 shows that during 23–24 July, a high-pressure system existed to the northeast of the TP, which hindered the movement of the TPV to the north. However, the background wind field in the region affected by the TPV only roughly indicated the movement direction of the TPV. For example, in the initial stage of the TPV moving off the TP, the average background wind field direction was northeast, and the average wind speed was 0.4 m s^{-1}, which was incon-

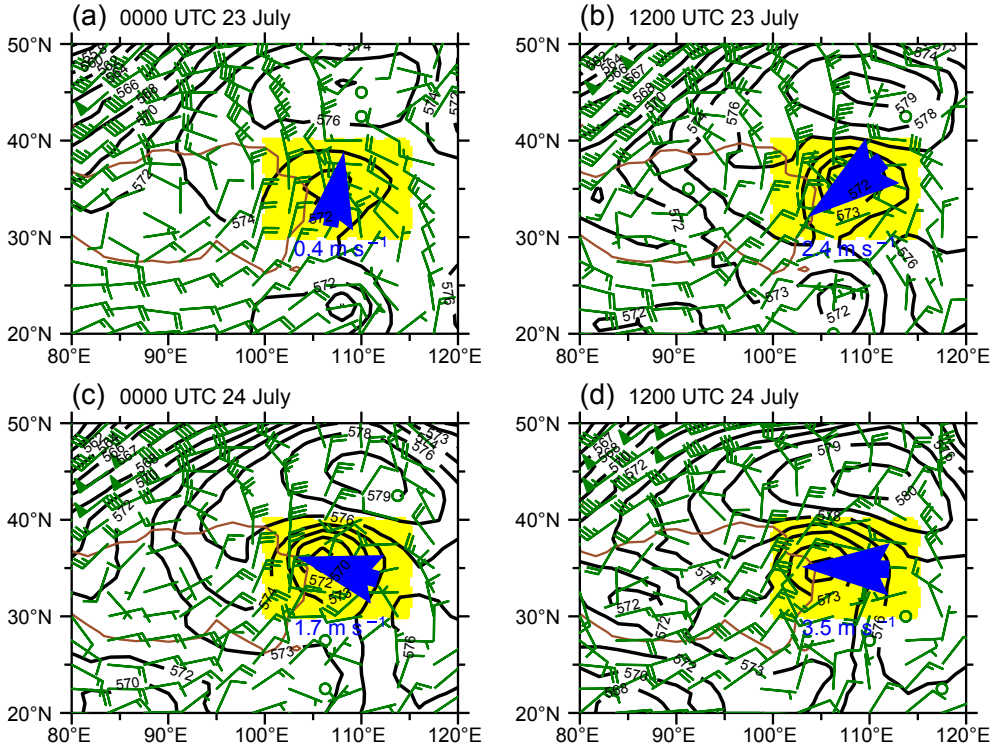

Fig. 12. Geopotential height (black solid line), area-averaged wind speed and direction (blue vector) in the active area (yellow square) of the TPV at 500-hPa, and the 200-hPa wind field (green barb) at (a) 0000 UTC 23 July 2010, (b) 1200 UTC 23 July 2010, (c) 0000 UTC 24 July 2010, and (c) 1200 UTC 24 July 2010. The topographic height threshold of 3 km above mean sea level (brown solid line) is shown.

sistent with the movement direction of the TPV. Comparatively, the directionality of the 200-hPa airflow during this period was relatively consistent with that of the TPV (Fig. 12a). Due to the development of the TPV, the wind field at 200-hPa after 1200 UTC 23 July also showed obvious cyclonic rotation characteristics, which weakened the indication of the movement direction of the TPV. In this period, the mean wind direction of the 500-hPa background wind field has a high correlation with the track of the TPV, but there were also deviations. At 0000 and 1200 UTC 24 July, the TPV moved to the southwest, but the average wind direction of the background wind field pointed to the northwest, and the average speed of the background wind field was much lower than that of the TPV (Figs. 12c, d). Therefore, we believe that the LCPV caused by LH significantly influenced the direction of movement of this TPV and can potentially serve as an important indicator for the tracks of TPVs in general.

To deduce the dominating factors of the LCPV, we analyzed the PV budget. When the friction term and residual term are ignored, the local change equation of PV is as follows:

$$\frac{\partial(\mathrm{PV})}{\partial t} \approx -\mathbf{V}\cdot\nabla(\mathrm{PV}) - \omega\frac{\partial(\mathrm{PV})}{\partial z} + \frac{\zeta}{\rho}\cdot\nabla\frac{\mathrm{d}\theta}{\mathrm{d}t}, \qquad (5)$$

where, on the right-hand side (from left to right) are the horizontal advection term (HAT), vertical advection term (VAT), and diabatic term (DT), respectively.

The key period for the occurrence of TPV-associated precipitation, the formation of the double arc-shaped precipitation region, and the change of the TPV's track were from 0000 UTC 23 July to 1200 UTC 24 July. Figure 13 shows the distribution of HAT, VAT, and DT at 500-hPa during this period, as well as the changing trend of the average value of LCPV, HAT, VAT, and DT near the TPV center. As can be seen from Figs. 13a–i, HAT and DT were the main factors leading to LCPV, while the contribution of VAT was relatively small.

In the early stage of the TPV moving off the TP, the key influence area of HAT was located to the northwest of the TPV center. As time goes by, the key influence area of HAT gradually shifted from the northwest to the southwest portion of the TPV center (Figs. 13a–d). Moreover, the absolute values of positive and negative centers of HAT were

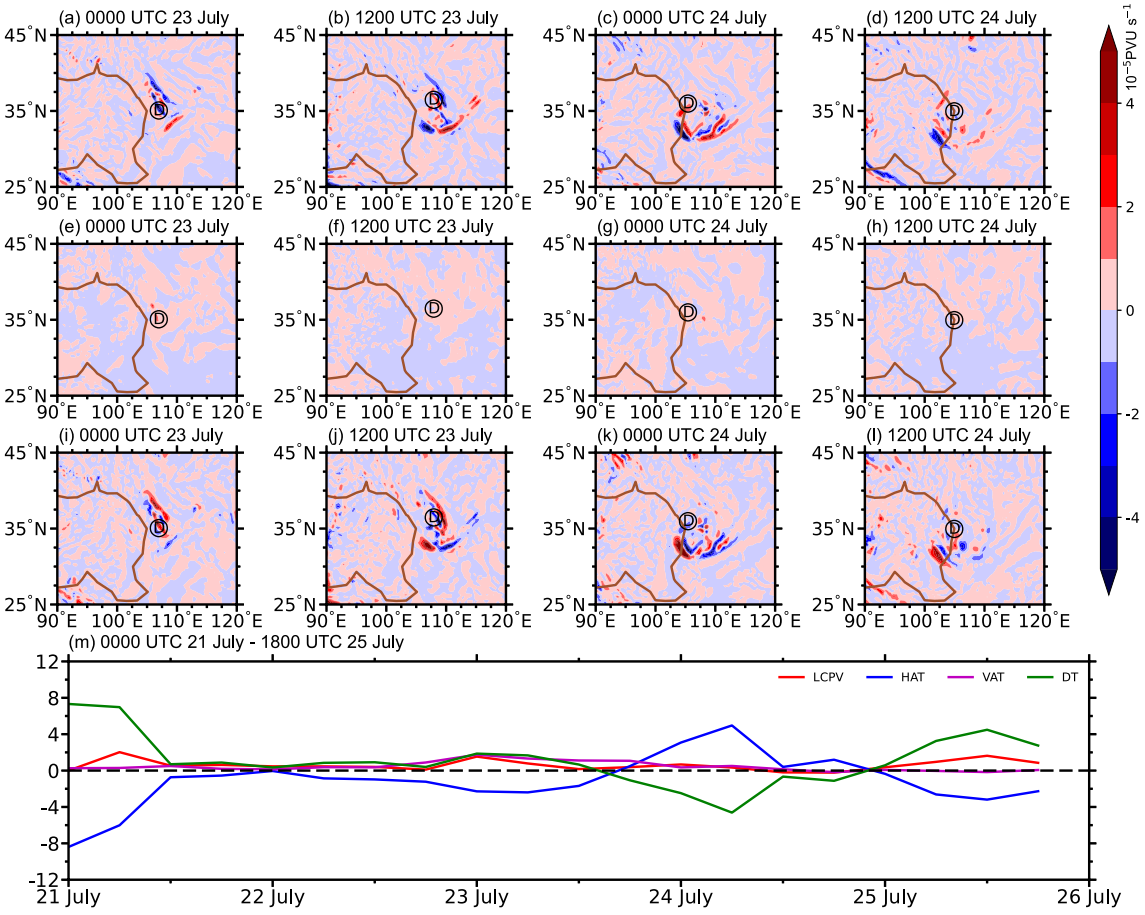

Fig. 13. Distribution of (a–d) HAT (units: 10^{-5} PVU s^{-1}), (e–h) VAT (units: 10^{-5} PVU s^{-1}), (i–l) DT (units: 10^{-5} PVU s^{-1}) at 500-hPa. (m) Time series of the regional (A square region with the TPV center as the center and a side length of 300 km) mean value of LCPV (black solid line), HAT (blue solid line), VAT (purple solid line), and DT (green solid line). The topographic height threshold of 3 km above mean sea level (brown solid line) is shown. The "D" represents the TPV and the "D" in the circle represents the location of the TPV center.

both more than 5×10^{-5} PVU s^{-1} in this process, which indicated that HAT had a very obvious effect on LCPV. It is worth noting that the distribution of HAT to the south of the TPV center showed an obvious arc-shaped feature (Figs. 13b–d) from 1200 UTC on 23 July, which proved that it was closely related to the circulation of the TPV. Similar to HAT, the key region affected by DT also transitioned from the northwest of the TPV center to the south of the TPV center with similar intensities. Since the corresponding region happened to be the main precipitation region associated with the TPV, we believe that the LH caused by precipitation played an important role in the distribution and intensity of DT. At 1200 UTC 24 July, the DT distribution showed an obvious double-arc-shaped distribution consistent with the TPV-associated precipitation region (Fig. 13l), and there was an obvious DT positive center to the south of the TPV center (HAT was negative in this region), which indicated that although the distribution and intensity of DT were similar to HAT, the increase of LCPV caused by DT was more conducive to the development of TPV in the southwest direction. It can also be seen from Fig. 13m that from 0000 UTC 21 July to 1800 UTC 25 July, the value of LCPV was most often greater than 0, and DT always positively contributed to the increase of LCPV until 1800 UTC 23 July. From 1200 UTC 24 July (The double-arc-shaped feature was most obvious in the precipitation region) to 1800 UTC 25 July, the mean DT value continued to increase (although it was negative before 0000 UTC 25 July), which was consistent with the trend of the mean value of LCPV. Considering that the trend of HAT was simultaneously opposite to that of LCPV, it is more reasonable to believe that DT was the dominant factor in LCPV variation during this period and that the distribution of DT played a more important role in the development of the TPV than the intensity.

Acknowledgements. This work was supported by the National Natural Science Foundation of China (Grant Nos. 42175002, 42030611, 42075013), the Natural Science Foundation of Sichuan, China (Grant No. 2023NSFSC0242), and the Innovation Team Fund of Southwest Regional Meteorological Center, China Meteorological Administration (Grant No. XNQYCXTD-202202).

REFERENCES

Chen, B. M., Z. A. Qian, and L. S. Zhang, 1996a: Numerical simulation of the formation and development of vortices over the Qinghai-Xizang Plateau in Summer. *Chinese Journal of Atmospheric Sciences*, **20**(4), 491–502, https://doi.org/10.3878/j.issn.1006-9895.1996.04.14. (in Chinese with English abstract)

Chen, F., and Coauthors, 1996b: Modeling of land surface evaporation by four schemes and comparison with FIFE observations. *J. Geophys. Res.: Atmos.*, **101**(D3), 7251–7268, https://doi.org/10.1029/95JD02165.

Chen, G., G. P. Li, and Y. Q. Li, 2012: The research progress of the Tibetan Plateau Vortex in recent twenty years. *Advances in Meteorological Science and Technology*, **2**(2), 6–12, https://doi.org/10.3969/j.issn.2095-1973.2012.02.001. (in Chinese with English abstract)

Dell'Osso, L., and S. J. Chen, 1986: Numerical experiments on the genesis of vortices over the Qinghai-Tibet Plateau. *Tellus A*, **38**(3), 236–250, https://doi.org/10.3402/tellusa.v38i3.11715.

Dong, Y. C., and G. P. Li, 2015: The structure and precipitation characteristics of typical Tibetan Plateau Vortices as revealed by energy analysis. *Chinese Journal of Atmospheric Sciences*, **39**(6), 1136–1148, https://doi.org/10.3878/j.issn.1006-9895.1502.14263. (in Chinese with English abstract)

Gao, D. M., Y. Q. Li, and X. L. Cheng, 2018: A numerical study on a heavy rainfall caused by an abnormal-path coupling vortex with the assimilation of southwest China vortex scientific experiment data. *Acta Meteorologica Sinica*, **76**(3), 343–360, https://doi.org/10.11676/qxxb2018.008. (in Chinese with English abstract)

Hersbach, H., and Coauthors, 2020: The ERA5 global reanalysis. *Quart. J. Roy. Meteor. Soc.*, **146**(730), 1999–2049, https://doi.org/10.1002/qj.3803.

Hong, S. Y., Y. Noh, and J. Dudhia, 2006: A new vertical diffusion package with an explicit treatment of entrainment processes. *Mon. Wea. Rev.*, **134**(9), 2318–2341, https://doi.org/10.1175/MWR3199.1.

Hoskins, B. J., M. E. McIntyre, and A. W. Robertson, 1985: On the use and significance of isentropic potential vorticity maps. *Quart. J. Roy. Meteor. Soc.*, **111**(470), 877–946, https://doi.org/10.1002/qj.49711147002.

Iacono, M. J., J. S. Delamere, E. J. Mlawer, M. W. Shephard, S. A. Clough, and W. D. Collins, 2008: Radiative forcing by long-lived greenhouse gases: Calculations with the AER radiative transfer models. *J. Geophys. Res.: Atmos.*, **113**(D13), D13103, https://doi.org/10.1029/2008JD009944.

Institute of Plateau Meteorology (IPM), and CMA, 2010: *Yearbook of Tibetan Plateau Vortex and Shear Line*. Science Press, Beijing, 1–113. (in Chinese)

Jiménez, P. A., J. Dudhia, J. F. González-Rouco, J. Navarro, J. P. Montávez, and E. García-Bustamante, 2012: A revised scheme for the WRF surface 1ayer formulation. *Mon. Wea. Rev.*, **140**(3), 898–918, https://doi.org/10.1175/MWR-D-11-00056.1.

Li, D., M. Liu, and H. Wang, 2008: Latent heat series over the east part of QXP in Rainy season and its impact on 500hPa height fields of northern hemisphere and precipitation in China flood season. *Plateau Meteorology*, **27**(4), 714–718. (in Chinese with English abstract)

Li, L., R. H. Zhang, and M. Wen, 2011: Diagnostic analysis of the evolution mechanism for a vortex over the Tibetan Plateau in June 2008. *Adv. Atmos. Sci.*, **28**(4), 797–808, https://doi.org/10.1007/s00376-010-0027-y.

Li, L., R. H. Zhang, M. Wen, and L. K. Liu, 2014: Effect of the atmospheric heat source on the development and eastward movement of the Tibetan Plateau vortices. *Tellus A*, **66**(1), 24451, https://doi.org/10.3402/tellusa.v66.24451.

Li, L., R. H. Zhang, M. Wen, and J. P. Duan, 2019: Development and eastward movement mechanisms of the Tibetan Plateau vortices moving off the Tibetan Plateau. *Climate Dyn.*, **52**(7–8), 4849–4859, https://doi.org/10.1007/s00382-018-4420-z.

Lin, Z. Q., W. D. Guo, L. Jia, X. P. Yao, and Z. B. Zhou, 2020: Climatology of Tibetan Plateau vortices derived from multiple reanalysis datasets. *Climate Dyn.*, **55**(7), 2237–2252, https://doi.org/10.1007/s00382-020-05380-6.

Lin, Z. Q., W. D. Guo, X. P. Yao, J. Du, W. K. Li, and J. Ge, 2021: Tibetan Plateau vortex-associated precipitation and its link with the Tibetan Plateau heating anomaly. *International Journal of Climatology*, **41**(14), 6300–6313, https://doi.org/10.1002/joc.7195.

Lin, Z. Q., X. P. Yao, W. D. Guo, J. Du, and Z. B. Zhou, 2022: Extreme precipitation events over the Tibetan Plateau and its Vicinity associated with Tibetan Plateau vortices. *Atmospheric Research*, **280**, 106433, https://doi.org/10.1016/j.atmosres.2022.106433.

Liu, F. M., and M. J. Fu, 1986: A study on the moving eastward lows over Qinghai-Xizang Plateau. *Plateau Meteorology*, **5**(2), 125–134. (in Chinese with English abstract)

Luo, S. W., 1989: Review of studies on weather and circulation in Qinghai-Xizang Plateau area. *Plateau Meteorology*, **8**(2), 121–126. (in Chinese with English abstract)

Luo, S. W., and Y. Yang, 1992: A case study on numerical simulation of summer vortex over Qinghai-Xizang (Tibetan) Plateau. *Plateau Meteorology*, **11**(1), 39–48. (in Chinese with English abstract)

Morrison, H., G. Thompson, and V. Tatarskii, 2009: Impact of cloud microphysics on the development of trailing stratiform precipitation in a simulated squall line: Comparison of one- and two-moment schemes. *Mon. Wea. Rev.*, **137**(3), 991–1007, https://doi.org/10.1175/2008MWR2556.1.

Shen, R., E. R. Reiter, and J. F. Bresch, 1986: Numerical simulation of the development of vortices over the Qinghai-Xizang (Tibet) Plateau. *Meteorol. Atmos. Phys.*, **35**(1–2), 70–95, https://doi.org/10.1007/BF01029526.

Shou S. W., 2010: Theory and Application of Potential Vorticity. *Meteorological Monthly*, **36**(3), 9–18, https://doi.org/10.7519/j.issn.1000-0526.2010.3.002. (in Chinese with English abstract)

Song, W. W., and G. P. Li, 2011: Numerical simulation and structure characteristic analysis of a plateau vortex process. *Plateau Meteorology*, **30**(2), 267–276. (in Chinese with English abstract)

Song, W. W., G. P. Li, and Q. K. Tang, 2012: Numerical simulation of the effect of heating and water vapor on two cases of plateau vortex. *Chinese Journal of Atmospheric Sciences*, **36**(1), 117–129, https://doi.org/10.3878/j.issn.1006-9895.2012.01.10. (in Chinese with English abstract)

Tian, S. R., A. M. Duan, Z. Q. Wang, and Y. F. Gong, 2015: Interaction of surface heating, the Tibetan Plateau vortex, and a convective system: A case study. *Chinese Journal of Atmospheric Sciences*, **39**(1), 125–136, https://doi.org/10.3878/j.issn.1006-9895.1404.13311. (in Chinese with English abstract)

Wang, W., Y. H. Kou, and T T. Warner, 1993: A diabatically driven mesoscale vortex in the Lee of the Tibetan Plateau. *Mon. Wea. Rev.*, **121**(9), 2542–2561, https://doi.org/10.1175/1520-0493(1993)121<2542:ADDMVI>2.0.CO;2.

Wu, D., F. M. Zhang, and C. H. Wang, 2018: Impacts of diabatic heating on the genesis and development of an inner Tibetan Plateau vortex. *J. Geophys. Res.: Atmos.*, **123**(20), 11 691–11 704, https://doi.org/10.1029/2018JD029240.

Xiao, Y. J., and L. P. Liu, 2006: Study of methods for interpolating data from weather radar network to 3-D grid and mosaics. *Acta Meteorologica Sinica*, **64**(5), 647–657, https://doi.org/10.11676/qxxb2006.063. (in Chinese with English abstract)

Xu, X. D., Y. J. Wang, T. L. Zhao, and W. Q. Yao, 2014: Relationship between turbulent energy in the near-surface layer and atmospheric boundary layer thermodynamic structure over the southeastern side of Tibetan Plateau. *Meteorological Monthly*, **40**(10), 1165–1173, https://doi.org/10.7519/j.issn.1000-0526.2014.10.001. (in Chinese with English abstract)

Yanai, M., C. F. Li, and Z. S. Song, 1992: Seasonal heating of the Tibetan Plateau and its effects on the evolution of the Asian summer monsoon. *J. Meteor. Soc. Japan*, **70**(1), 319–351, https://doi.org/10.2151/jmsj1965.70.1B_319.

Yao, X. P., and J. Y. Sun, 2013: The thermal forcing analysis of the impact of the easterlies vortex on the subtropical anticyclone over the western Pacific east-west shift. *Journal of Tropical Meteorology*, **29**(4), 551–558, https://doi.org/10.3969/j.issn.1004-4965.2013.04.003. (in Chinese with English abstract)

Yao, X. P., and J. Y. Sun, 2016: Thermal forcing impacts of the easterly vortex on the east-west shift of the subtropical anticyclone over western Pacific Ocean. *Journal of Tropical Meteorology*, **22**(1), 51–56, https://doi.org/10.16555/j.1006-8775.2016.01.006.

Ye, D. Z., 1979. *Tibetan Plateau Meteorology*. Science Press, Beijing, 7–8. (in Chinese)

Yu, S. H., and W. L. Gao, 2019: Characteristics of surface Land heating in the Qinghai-Tibetan Plateau vortex source regions along with the departure plateau vortex and non-departure plateau vortex. *Plateau Meteorology*, **38**(2), 299–313, https://doi.org/10.7522/j.issn.1000-0534.2018.00086. (in Chinese with English abstract)

Yu, S. H., W. L. Gao, and Q. Y. Gu, 2007: The middle-upper circulation analyses of the plateau vortex moving out of plateau and influencing flood in east China in recent years. *Plateau Meteorology*, **26**(3), 466–475, https://doi.org/10.3321/j.issn:1000-0534.2007.03.005. (in Chinese with English abstract)

Zhang, P. F., G. P. Li, X. H. Fu, Y. M. Liu, and L. F. Li, 2014: Clustering of Tibetan Plateau vortices by 10–30-day intraseasonal oscillation. *Mon. Wea. Rev.*, **142**(1), 290–300, https://doi.org/10.1175/MWR-D-13-00137.1.